Assessment of Numerical Weather Models With Different Spatial Resolutions on Tropospheric Delay Correction for InSAR

Yongchao Ma, Tong Liu, Zhibin Yu, Chaowei Jiang, and Zhiping Lu

***Abstract*—Spatial variations in atmospheric parameters, including pressure, temperature, and humidity, significantly impact the precision of interferometric synthetic aperture radar (InSAR) measurements. This significantly limits the applicability of InSAR in the fields, such as terrain inversion and deformation monitoring. Fortunately, the evolving numerical weather models (NWMs) could offer a viable tropospheric correction solution. However, given the influence of complex terrain and areas with sparse atmospheric observation, the effectiveness of tropospheric correction with different NWMs' resolutions remains to be evaluated. This requires the examination of different NWMs tropospheric delay correction in detail with sufficient metrics. A total of 36 Sentinel-1 interferograms of 2023, which cover Berlin, Paris, and Milan, respectively, are used as examples. Tropospheric correction is carried out using ICOsahedral nonhydrostatic D2 (ICON-D2), the fifth-generation European Centre for Medium-Range Weather Forecast atmospheric reanalysis, and modern-era retrospective analysis for research and applications version 2. To assess the correction efficacy of various resolutions, standard deviation, semivariogram function, and phase–elevation correlation coefficient served as the evaluation method. Results show that the ICON-D2 model outperforms the other models in these metrics, especially in regions with significant topographic relief. Among them, the standard deviation of the corrected interferogram decreased by 21.6%–35.8%. NWMs have demonstrated effectiveness in mitigating altitude-related tropospheric delays without needing altitude assimilation. Overall, the present study underscores that despite potential uncalibrated atmospheric effects, high-resolution NWMs are anticipated to provide a more precise solution for InSAR, especially in regions exhibiting intricate and challenging terrain features.**

***Index Terms*—Interferometric synthetic aperture radar (InSAR), numerical weather models (NWMs), tropospheric correction.**

Manuscript received 7 February 2024; revised 26 June 2024; accepted 30 July 2024. Date of publication 8 August 2024; date of current version 15 August 2024. This work was supported by the Key-Area Research and Development Program of Guangdong Province under Grant 2020B0303020001. *(Corresponding author: Zhibin Yu.)*

Yongchao Ma, Zhibin Yu, and Chaowei Jiang are with the Institute of Space Science and Applied Technology, Harbin Institute of Technology (Shenzhen), Shenzhen 518055, China (e-mail: ma_yongchao@stu.hit.edu.cn; yuzb@hit.edu.cn; chaowei@hit.edu.cn).

Tong Liu is with the Department of Land Surveying and Geo-Informatics, The Hong Kong Polytechnic University, Hong Kong (e-mail: tong2.liu@polyu.edu.hk).

Zhiping Lu is with the Information Engineering University, Zhengzhou 450001, China (e-mail: ssscenter@126.com).

Digital Object Identifier 10.1109/JSTARS.2024.3440648

I. Introduction

INTERFEROMETRIC synthetic aperture radar (InSAR) offers the ability to measure surface topography with all-weather capabilities, high resolution, and extensive coverage [1]. Thus, it has indispensable utility [2] in geodetic applications, such as monitoring volcanic activities [3], [4], [5] and tracking surface subsidence and landslide events [6], [7]. During the propagation of the signal, tropospheric delay constitutes a notable source of error and poses a significant constraint on the signal range and inversion quality of spaceborne repeat-pass InSAR measurements [8]. This limitation arises because electromagnetic wave signals experience variations in tropospheric temperature, pressure, and humidity during atmospheric propagation. The signal propagation speed varies with the refractive index, leading to different degrees of phase delay [9]. Studies have demonstrated that spatial and temporal fluctuations in relative humidity, even at 20%, can result in a substantial 10 cm deformation measurement error [10]. How to mitigate the effects of tropospheric delay is a continuing challenge for achieving high-precision surface monitoring in InSAR applications.

In general, InSAR tropospheric delay can be reduced by correction methods, broadly categorized into two types: correction utilizing the interferogram's inherent features and correction through the introduction of external atmospheric products.

The first approach primarily encompasses two strategies: First, leveraging the correlation between the interferometric phase and the topography, employing linear or power–law relationships to mitigate vertical stratified delays, and second, utilizing stacking or filtering techniques to eliminate the effects of atmospheric turbulence. Among these, the tropospheric correction based on filtering typically presupposes that the tropospheric errors exhibit high spatial correlation but low temporal correlation. This issue is adeptly addressed through the synergistic application of spatial and temporal filters, which effectively refines the atmospheric delay correction process. The former often assumes that atmospheric errors exhibit high spatial correlation but low temporal correlation, addressing them through a combination of spatial and temporal filters. However, in many cases, this assumption proves to be inaccurate.

Comparatively, tropospheric correction methods relying on external data offer a more straightforward approach by providing comprehensive information on tropospheric delay. These external data sources primarily encompass global navigation

satellite system (GNSS) [11], [12], medium-resolution imaging spectrometer [13], [14], moderate resolution imaging spectroradiometer (MODIS) [15], [16], and data derived from global atmospheric numerical models, including reanalysis models, such as ERA5 and modern-era retrospective analysis for research and applications version 2 (MERRA2) [17], [18], as well as numerical weather prediction models (MM5 and WRF) [19], [20]. Additionally, there are GACOS data that fuse GNSS and European Centre for Medium-Range Weather Forecast (ECMWF) data [21]. Even with so much external data available, the spatial and temporal resolution, as well as the accuracy of external data, poses key limitations for InSAR tropospheric delay correction [22]. This is due to the fact that the majority of external data sources have shortcomings. For instance, GNSS and reanalysis data suffer from low spatial and temporal resolution, respectively; whereas MODIS products exhibit high spatial resolution but very low temporal resolution and are significantly influenced by cloud cover, requiring correction for reliable use [23]; GACOS relies on assumptions about atmospheric properties and is constrained by the resolution of the ECMWF. Furthermore, the runtime and accuracy of numerical weather prediction models are limited by factors, such as initial fields, boundary conditions, and microphysical schemes.

Fortunately, as a usual external tropospheric correction way, numerical weather models (NWMs) offer resolution-specific and spatially complete external data, validated and employed in various studies. For instance, Jolivet et al. [24] validated the efficacy of NWMs for single interferogram and time-series analysis in Southern California, highlighting the significant potential of NWMs for InSAR tropospheric correction. In an assessment of NWMs' performance in InSAR tropospheric correction, Wang et al. [25] utilized ERA5, ERA-I, MERRA2, and GACOS for correcting tropospheric phase delay in InSAR over the Tibetan Plateau. The results indicated the effectiveness of global atmospheric models (GAMs) in atmospheric phase screen (APS) correction, with ERA5 and GACOS products demonstrating similar and generally superior performance compared with other types. This underscores the significant potential of GAM, especially ERA5, in APS correction for InSAR applications on the Tibetan Plateau. Building on this, Zhang et al. [18] further investigated the usability of NWMs by testing ERA5 and ERA-I in China. The results highlighted a strong correlation between the correction effects of these reanalysis data and terrain undulation, in addition to seasonal effects. Cao et al. [26] adopted a computed line-of-sight path delay approach based on ERA5, integrating a stochastic model to overcome errors associated with atmospheric anisotropy. This approach significantly improved over conventional methods. In a study by Zhao et al. [27], it was concluded that the linear correction method proves useful in low-latitude regions with high terrain undulation. Specifically, the linear correction method emerged as the most effective for InSAR tropospheric correction in low-latitude areas with substantial topographic relief, followed by GACOS, while ERA5 exhibited comparatively poor correction stability.

Despite the considerable research on tropospheric correction methods with NWMs, the evaluation of their performance remains a prevalent research focus. Especially, NWMs are continually advancing with higher resolutions and enhanced performance, particularly in the case of regional models. For instance, the ICOsahedral nonhydrostatic D2 (ICON-D2) model, covering parts of Europe, boasts a temporal and spatial resolution of 1 h and 0.02°, respectively. However, the present study lacks a comprehensive assessment of ICON-D2 data in InSAR tropospheric correction and an exploration of the impacts of different resolution NWMs in tropospheric correction. Moreover, many analyses involve a limited number of interferograms and often lack uniform evaluation metrics. Typically, simpler metrics, such as the overall variance, of individual interferograms are employed. This approach may be insufficient, given the need for metrics that effectively assess whether atmospheric phase correction enhances or degrades interferograms, especially in regions with complex meteorology and relatively sparse observations [28]. Consequently, a more thorough investigation is necessary to address these gaps and enhance our understanding of the effectiveness of different resolution NWMs in InSAR tropospheric correction, ensuring the robustness of predictions in regions with intricate meteorological conditions and sparse observational data.

Building upon the aforementioned considerations, this study delves into tropospheric delay correction within three distinct sampling regions, encompassing Milan, Paris, and Berlin. The selected study areas offer a diversity of seasons and varying terrain reliefs. To comprehensively assess the applicability of ICON-D2, ERA5, MERRA2, and GACOS for tropospheric delay correction in InSAR, representative metrics have been employed. These metrics include the phase standard deviation (STD), providing an assessment of the overall performance of the corrections, the spatial structure function, evaluating the reduction of long-wave atmospheric effects, and the phase–elevation correlation coefficient, measuring the reduction of the stratified component of tropospheric delay. The rest of this article is organized as follows. Section II will present the InSAR and NWMs data used along with the methodology. Subsequently, Section III will unveil the correction results and engage in pertinent discussions. Finally, Section IV concludes this article.

II. Data and Method

A. Study Area and Data Preprocessing Strategy

In consideration of the geomorphic distinctions, geographic locations, and coverage of ICON-D2, Berlin, Germany, Milan, Italy, and Paris, France were chosen as regions of interest to assess the impact of different resolution NWMs in InSAR tropospheric correction, as depicted in Fig. 1. Among them, Paris and Berlin have relatively flat terrain, while the Milan region has a more complex terrain. By comparing the two regions with similar terrain, Paris and Berlin, this study can explore the effect of NWMs correction in the horizontal direction more deeply. A total of 36 interferograms were generated by selecting Sentinel-1A SAR images on both 1 January 2023 and 31 December 2023. Given a temporal baseline of 12 days for each interferogram pair, the associated terrain deformation was deemed negligible. To investigate the effects of tropospheric delay correction across various spatial scales, the complete

TABLE I
INFORMATION OF SELECTED INTERFEROGRAMS

Berlin	Reference	Secondary	Paris	Reference	Secondary	Milan	Reference	Secondary
IF01	20230206	20230218	IF01	20230212	20230224	IF01	20230213	20230225
IF02	20230302	20230314	IF02	20230308	20230320	IF02	20230309	20230321
IF03	20230326	20230407	IF03	20230401	20230413	IF03	20230402	20230426
IF04	20230419	20230501	IF04	20230425	20230507	IF04	20230508	20230520
IF05	20230513	20230525	IF05	20230519	20230531	IF05	20230601	20230613
IF06	20230606	20230618	IF06	20230612	20230624	IF06	20230625	20230707
IF07	20230630	20230712	IF07	20230706	20230718	IF07	20230719	20230731
IF08	20230724	20230805	IF08	20230730	20230811	IF08	20230812	20230905
IF09	20230817	20230829	IF09	20230823	20230904	IF09	20230917	20230929
IF10	20230910	20230922	IF10	20230916	20230928	IF10	20231011	20231023
IF11	20231016	20231028	IF11	20231010	20231022	IF11	20231104	20231116
IF12	20231109	20231121	IF12	20231103	20231115	IF12	20231128	20231210

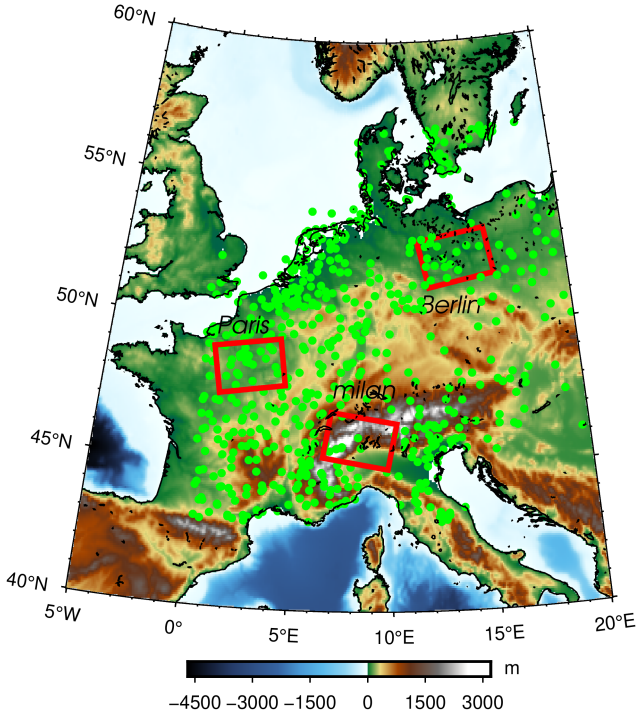

Fig. 1. Topography of the study area and distribution of GNSS stations. The red box identifies the coverage of the interferograms.

content of each interferogram was retained, with their latitude and longitude spatial spans exceeding 1°. Table I provides details for the 36 pairs of interferograms.

The interferograms were created using the InSAR scientific computing environment software [29], with precision orbits from the Copernicus precision orbit determination service aiding in SAR image alignment, baseline error reduction, and terrain phase removal. The USGS SRTM DEM was utilized to reproduce and eliminate the terrain phase component from the interferograms. Further processing involved unfolding the interferograms using the ICU [30] and SNAPHU software packages [31]. To facilitate subsequent data computation and minimize complexity, a 20 × 5 multilook operation was conducted in both the distance and azimuth directions.

B. Numerical Weather Model

To thoroughly investigate the impact of different resolution NWMs in InSAR tropospheric correction, this study selected ICON-D2, ERA5, and MERRA2 as the test datasets. To enhance the comprehensiveness of the evaluation, the GACOS product was employed on three representative interferograms, allowing for a comparative analysis with the test products. Additionally, temporal linear interpolation was applied between the two outputs spanning the SAR acquisition time to more effectively address temporal variations in the troposphere.

1) ERA5: ERA5 is the most recent reanalysis dataset provided by the ECMWFs, encompassing both surface and pressure layer data and distinguished by global coverage and temporal continuity [32]. This dataset boasts a temporal resolution of 1 h and a spatial resolution of 0.25°. The pressure layer dataset comprises 37 vertical layers spanning the pressure range from 1000 to 1 hPa. Tropospheric delay derived from the ERA5 pressure layers exhibits high accuracy. In the current study, we leverage the ERA5 pressure layer dataset, aligned temporally with SAR acquisition, to extract four meteorological factors—temperature, geopotential, specific humidity, and pressure—for the computation of zenith total delay (ZTD). The original data can be accessed through the website.[1]

2) MERRA2: MERRA2 data represent the latest generation of global atmospheric reanalysis information provided by NASA.[2] This dataset signifies an enhancement in quality compared with the previous MERRA atmospheric reanalysis data. MERRA2 includes surface meteorological parameters and stratified meteorological data, featuring a horizontal resolution of 0.5° × 0.625° and a vertical resolution comprising 42 baroclinic layers up to 0.1 hPa. The temporal resolution for the pressure layer data is 6 h, while the surface data operate at a temporal resolution of 1 h. The ZTD generated by MERRA2 has been validated to exhibit high accuracy [33], comparable with the results obtained from ERA5. In this experiment, we acquired

[1][Online]. Available: https://cds.climate.copernicus.eu/cdsapp#!/dataset/reanalysis-era5-single-levels?tab=overview

[2][Online]. Available: https://goldsmr4.Gesdisc.eosdis.nasa.gov/data/MERRA2

tropospheric delay maps based on the meteorological data from the pressure layer, aligning temporally with the SAR acquisition.

3) GACOS: GACOS offers a freely accessible, globally covered ZTD product designed for InSAR tropospheric delay correction [34]. It incorporates a 6-h interval, 0.125° grid, and 137-level vertical resolution ECMWF data, assimilating them with continuous GPS tropospheric delay estimates through the iterative tropospheric decomposition model [35]. The product boasts a temporal resolution of 1 min and a spatial resolution of 90 m. Users can download this data from the web by visiting the link.[3]

4) ICON-D2: The modeling framework of the ICOsahedral nonhydrostatic (ICON) was collaboratively developed by the German Weather Service (DWD) and the Max Planck Institute for Meteorology to create a unified, next-generation global numerical weather prediction and climate simulation system. ICON utilizes an unstructured triangular mesh based on the successive refinements of the spherical icosahedron, composed of 20 equilateral triangles of equal size [36]. The detailed data information can be accessed on the official website.[4] In this study, the regional ICON-D2 model, nested within the global ICON model, was utilized. The horizontal resolution employed was 0.02° × 0.02°, with 65 vertical model layers extending up to 20 km. The temporal resolution was set at 1 h. Although GNSS ZTD and radio occultation data have been assimilated into the ICON global model, it should be noted that this assimilation has not yet been incorporated into the nested regional model.

The ERA5 and MERRA2 models offer refractive index values at high altitudes (1 hPa or 0.1 hPa pressure layers), eliminating the need to calculate the refractive index above the top of the model. However, for limited-area NWMs, such as ICON-D2, the top of the model is situated at an altitude of 20 km. To address potential errors arising from extrapolated interpolation, we adopted an approach employed by previous researchers [37]. Assuming negligible humidity and a constant temperature above the top of the model, the pressure was derived from the hydrostatic equation. Subsequently, the refractive index (N) at the geopotential height (H) is determined by the equation

$$N = N_0 \cdot \exp\left(-\mathrm{GMR}\frac{H - H_0}{T_0}\right) \tag{1}$$

where N_0, T_0, and H_0 represent the refractive index, temperature, and potential height at the top of the model, respectively. Additionally, GMR denotes the hydrostatic constant. Further details on this equation can be referenced in the literature [37].

In this study, a dataset comprising 500 GNSS stations across Europe in the year 2023 is utilized as a reference to validate the ZTD accuracy of the ICON-D2 model solution, as shown in Fig. 1. Table II presents the accuracy statistics of ZTD generated by NWMs, validated against GNSS ZTD. The statistical analysis shows an average root-mean-square error (RMSE) of 9.3 mm. The ZTD accuracy, as determined by the three distinct NWMs, is on par, with an approximate precision of 1 cm.

[3][Online]. Available: http://www.gacos.net/

[4][Online]. Available: https://www.dwd.de/EN/research/weatherforecasting/num_modelling/01_num_weather_prediction_modells/icon_description.html

TABLE II
ACCURACY STATISTICS OF DIFFERENT MODELS DERIVED ZTD AGAINST GNSS ZTD (UNIT: CM)

	Bias			RMSE		
	Min	Max	Mean	Min	Max	Mean
ERA5	-8.49	5.31	0.51	0.52	2.18	1.01
MERRA2	-5.52	5.77	0.55	0.54	2.98	1.06
ICON-D2	-5.68	4.88	0.14	0.37	2.47	0.93

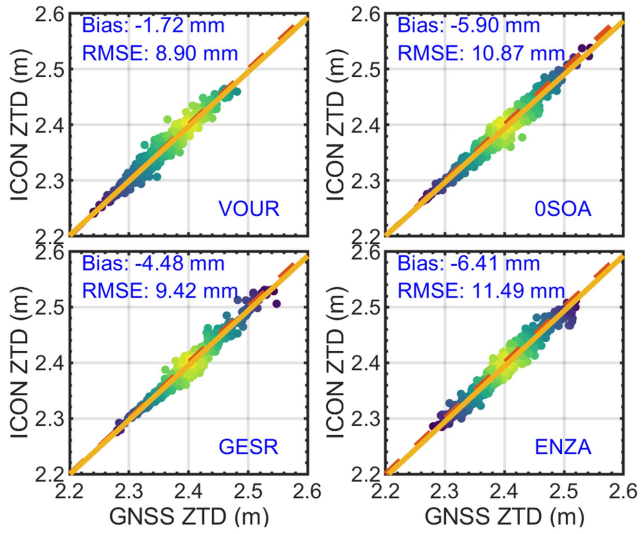

Fig. 2. Scatter plots of GNSS ZTD versus modeled values of ICON-D2 for 2023.

Fig. 2 visually presents a comparison of ZTD values from different sources for four randomly selected stations. Notably, the GNSS ZTDs for these stations exhibit a high level of agreement with the ICON-D2 ZTD. The bias and RMSE for these stations are all less than 1 cm when compared with the GNSS ZTD. The results affirm the reliability of ZTD estimates derived from the ICON-D2 solution, demonstrating a comparable level of accuracy to ERA5 and MERRA2. The three test datasets, possessing equivalent accuracy, provide a robust basis to assess the influence of different resolutions in InSAR tropospheric correction by NWMs.

C. Methodology

1) NWMs Based Tropospheric Correction Method for InSAR: Tropospheric delay in InSAR is the outcome of electromagnetic wave refraction caused by variations in temperature, pressure, and humidity as the waves traverse the troposphere. This delay is primarily composed of a wet component, influenced by water vapor and temperature, and a dry component, influenced by air pressure and temperature. In the context of InSAR, the atmospheric refraction's variability during the two repeated orbit data acquisitions leads to residual atmospheric phase delay in the interferograms. This phenomenon introduces complexities in the geophysical interpretation of the images. Despite the hydrostatic delay's greater magnitude compared with the wet component for a specific date, the wet component exerts a more substantial

impact on the interferogram than the hydrostatic component. Due to the relatively stable nature of ZHD over short periods, its contribution to the residuals after the difference is minimal. In contrast, ZWD exhibits significant variation between two observations, so it dominates the residual tropospheric delay phase after the difference.

The atmospheric phase difference for a single SAR data observation can be expressed as follows:

$$\phi_{\text{atm}} = \frac{-4\pi}{\lambda} \cdot \frac{10^{-6}}{\cos(\theta)} \int_{h_0}^{h_{\text{top}}} N(h)dh \tag{2}$$

where λ is the radar wavelength, θ is the radar incidence angle, N is the refractive index, and h_0, and h_{top} denote the bottom and top layers of the troposphere, respectively. Given that the incidence angle θ of the Sentinel-1 satellite is approximately between 30° and 45°, the mapping function can be approximated as a cosine function [38]. Calculating the delay from the zenith allows for cubic spline interpolation in the vertical direction and bilinear interpolation in the horizontal direction. This composite method has demonstrated effectiveness and has been validated in various geographic and tectonic environments.

The unwrapped phase is obtained by first differentiating the two observation data to form an interferogram, and then phase unwrapping the interferogram, which can be expressed as follows:

$$\phi_{\text{diff}} = \left(\phi_{\text{atm}}^{t2} - \phi_{\text{atm}}^{t1}\right) + \phi_{\text{def}} + \phi_{\text{noise}} \tag{3}$$

where φ_{def} represents the surface displacement and φ_{noise} represents the other noise sources, such as ionospheric error, detangling error, and thermal noise.

The accurate calculation of tropospheric delay in interferograms relies on the precise computation of ZTD that aligns with both the time and region of the interferograms. Global and regional atmospheric reanalysis data offer atmospheric variables, including temperature, geopotential, pressure, and specific humidity, at a relatively high spatial and temporal resolution. The process involves obtaining refractive indices between each pressure layer based on the atmospheric parameters of the modeled pressure layers. These refractive indices are then interpolated to altitude based on the height of the pressure layer. Finally, the refractive indices between a specific pressure layer and the top layer are integrated to obtain the tropospheric delay. The specific formula for the atmospheric refractive index is given as follows [39]:

$$N = N_{\text{dry}} + N_{\text{wet}} = \frac{k_1(P-e)}{T} + \frac{k_2 e}{T} + \frac{k_3 e}{T^2} \tag{4}$$

where N_{dry} and N_{wet} denote the atmospheric refractive indices for hydrostatic and wet delay, respectively. P is the atmospheric pressure, and e represents the water vapor partial pressure. $k_1 = 0.776\ \text{K}\cdot\text{Pa}^{-1}$, $k_2 = 0.716\ \text{K}\cdot\text{Pa}^{-1}$, and $k_3 = 3.75 \times 10^3\ \text{K}^2\cdot\text{Pa}^{-1}$.

2) Indicators for Assessing the Quality of Corrections: In this article, the quality of correction is assessed using STD, spatial semivariogram, and phase–elevation to verify the correction effect of each numerical model. STD serves as a reliable metric for gauging the dispersion of the unwrapped phase after correction using various methods

$$\text{STD} = \sqrt{\frac{1}{M-1}\sum_{i=1}^{M}\left(\phi_{\text{corr}_i} - \bar{\phi}_{\text{corr}}\right)} \tag{5}$$

where ϕ_{corr_i} ($i = 1, 2, 3, \ldots, M$) is the corrected M interferogram unwrapped phases, and $\bar{\phi}_{\text{corr}}$ is the average of the corrected phases.

To assess the STD of interferograms before and after correction across various spatial scales, this study adopted a methodology wherein, for each window, the average of the STDs from 200 subinterferograms was randomly sampled as the final result. As the window size approaches the image size, the range of 200 pans for a given window size becomes more constrained. Larger windows, however, can sample a greater number of redundant pixels. This approach proves more effective in capturing tropospheric changes before and after correction compared with a simple average of the spatial variance of individual interferograms [40].

As tropospheric phases exhibit spatial correlation, the semivariogram is employed for quantitative analysis of the reduction in spatially correlated signals after tropospheric correction. The semivariogram, also referred to as the spatial structure function, is a mathematical function that describes the variability of the data in relation to the distance between the pairs of data points [41]. This function enables a clear distinction of the correction effects on various spatial scales and is not constrained by the presence of gaps or irregularly spaced data points. The semivariogram is defined as follows:

$$S(r) = E\left[\left(\phi_{\text{corr}}(x) - \phi_{\text{corr}}(x+r)\right)^2\right]. \tag{6}$$

The semivariogram characterizes the spatial correlation among pairs of sample points. Typically, this function exhibits values at a certain distance (range) that approach the maximum and then flatten out, indicating a lack of correlation beyond that distance. The square root of the sill is equivalent to the rms of the interferogram. For datasets containing signals on large spatial scales, such as those from orbital errors or significant atmospheric effects, the semivariogram value may continue to increase on scales comparable to or larger than the interferogram size, without reaching a sill. Researchers commonly eliminate the planar function from the image before computing the semivariability function to weed out large-scale spatial signals.

To conduct a comprehensive comparison of the correction effects across various scales, this study employs an identical approach to that utilized in the referenced literature [40]. The only operation performed is the removal of the mean value from each interferogram, with no other functions being eliminated. Residual signals with large spatial scales may persist due to unmodeled tropospheric, ionospheric, and/or orbital effects, or signals introduced by errors in the tropospheric model.

III. Result

Based on the validation method outlined in Section II, this section proceeds to validate and discuss the tropospheric correction effects of different NWMs in three representative regions.

TABLE III
STATISTICAL INFORMATION OF CORRECTING RESULTS FROM DIFFERENT NWMS (UNIT: RAD)

	Original	GACOS	ERA5	ICON-D2	MERRA2
phase (Berlin)	5.30	3.86	3.86	3.40	3.57
NISD		10	9	11	10
phase (Paris)	4.99	3.35	3.68	3.50	4.18
NISD		9	8	8	7
phase (Milan)	4.77	3.70	4.04	3.74	3.80
NISD		10	9	10	9

The experiments are conducted in three areas, considering variations in time, characteristics of spatial distribution, and elevation changes.

A. Overall NWMs Correction Effect

Table III provides the average STD of all interferograms before and after tropospheric correction, along with the number of interferograms with reduced standard deviations (NISD) after correction. On the whole, the interferograms are corrected to some extent through the NWMs correction method. Notably, the ICON-D2 model exhibits better correction than ERA5 and MERRA2 in all regions, comparable with the accuracy of GACOS, with some interferograms even demonstrating superior correction compared with GACOS. Considering the topography, it becomes apparent that the STD of interferograms in mountainous regions (Milan) is significantly lower than those in urban regions (Paris and Berlin). In terms of STD reduction, NWMs do not correct as effectively in mountainous areas as in urban areas. From the individual case data, it is observed that the atmospheric numerical model did not consistently achieve effective correction for all interferograms and, in some cases, introduced more errors. Notably, the percentage of effective correction for ICON-D2 is 80.56%, surpassing that of ERA5 and MERRA2. The cumulative percentage of correction for STD error reduction reveals a significant difference between the four methods.

Fig. 3 illustrates the STD of a series of interferograms for three regions before and after tropospheric correction using different NWMs. Observations from the figure reveal that the STDs of precorrection interferograms are notably higher in summer compared with other seasons, peaking around July. This is attributed to increased water vapor and heightened atmospheric activity during summer, causing a more significant influence on radar signals compared with other seasons. In areas where the terrain changes significantly, the vertical stratified delay part related to the terrain height will dominate; while in areas with flat terrain, the effect of the turbulence component will be more significant. Fig. 3(c) shows that the NWMs corrected STD curves do not have more prominent anomalous changes in summer. This may be because the vertical component of the troposphere, which is altitude dependent, is the active factor in the complex terrain region. During the summer months when water vapor is active, the vertical stratification delay volume

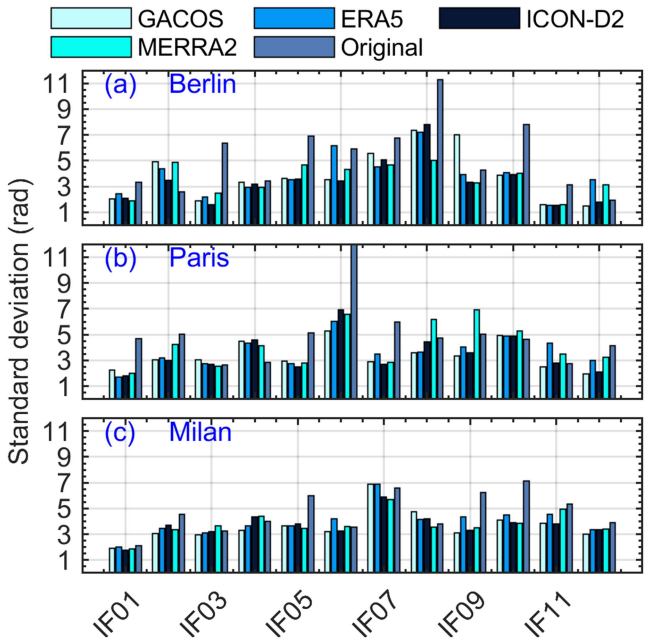

Fig. 3. Tropospheric correction effects for different cases based on different NWMs.

does not affect the interferogram as much as the turbulence component. In contrast, the effect of tropospheric delay correction in urban areas depends mainly on the ability of the atmospheric model to capture turbulent delays. In the Paris region, the overall correction effects of ICON-D2 and GACOS are comparable and superior to those of ERA5 and MERRA2, while in the Berlin region, the ICON-D2-based correction is the most effective, followed by MERRA2. This suggests that there is regional variability in the effects of the NWMs based correction.

A comparison of the corrections of all interferograms revealed that the correction by NWMs did not demonstrate all positive corrections. For example, Berlin: IF02; Paris: IF04, IF10; and Milan: IF08, all show that the NWMs corrected STD is larger than the precorrection. For urban areas, due to the complexity of the turbulent delays and the fact that the current resolution models do not correctly invert the small-scale variations in the delays, there are deviations from the true atmospheric state that introduce new errors when corrected by the NWMs. In addition, the spatial distribution characteristics of elevation-dependent vertical stratification delays are often not adequately captured when correcting areas with high relief based on low-resolution NWMs. When processed by spatial interpolation techniques, such methods may introduce additional errors, which are particularly significant in the presence of high terrain relief or extreme weather conditions. In summary, the tropospheric delays provided by high-resolution atmospheric models are more conducive to InSAR phase correction of tropospheric delays with equal accuracy.

B. Assessment and Analysis of Regional Correction Effect

It is known from the previous section that NWMs do not always perform forward correction. To analyze the impact

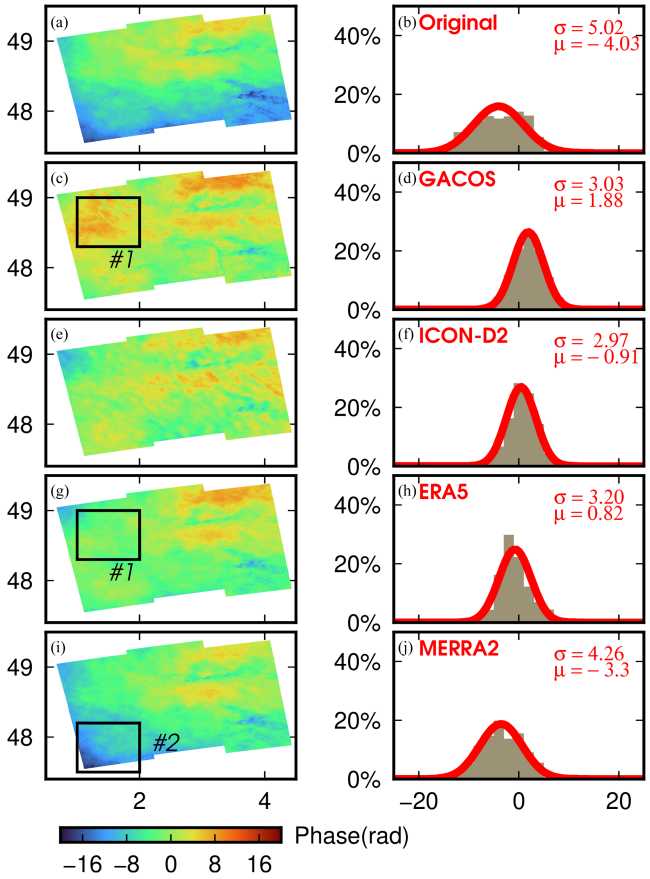

Fig. 4. Distribution of interference phases before and after tropospheric correction using different methods in Paris.

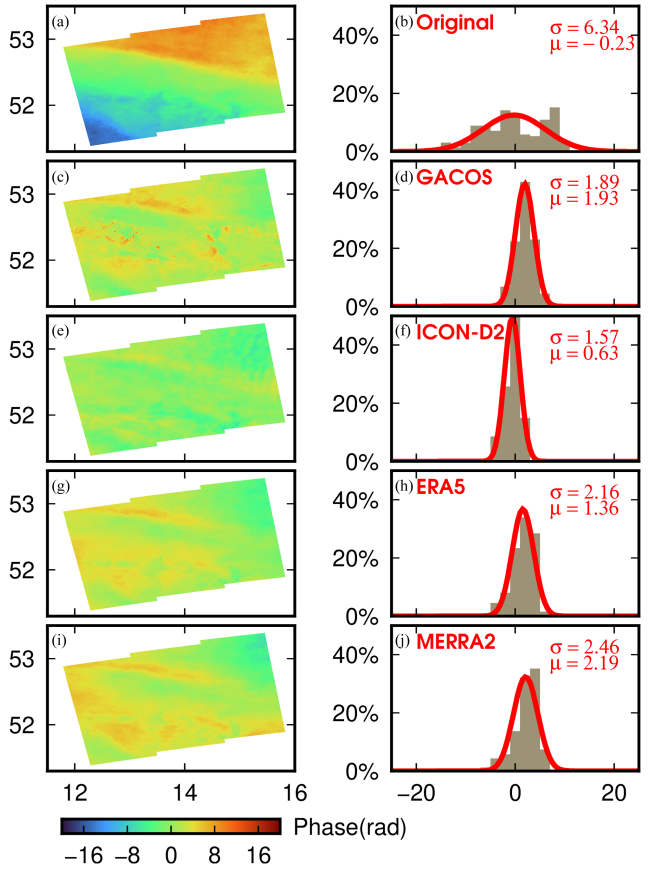

Fig. 5. Distribution of interference phases before and after tropospheric correction using different methods in Berlin.

of NWMs resolution differences on correcting the InSAR troposphere, this study selects interferograms positively corrected by the NWMs as examples to examine the spatial characteristics of the residual phases.

1) Correction Results in Paris: Fig. 4 displays the residual phase distribution of case IF02 covering the Paris area before and after correction using different atmospheric models. Overall, the interferograms corrected with various correction methods exhibit significant improvement compared with the original interferograms. Notably, the ICON-D2 method outperforms similar models across the entire domain and even slightly surpasses the GACOS method. The mean values and STD of the corrected interferograms based on GACOS, ICON-D2, ERA5, and MERRA2 models are reduced by 53.3%/39.6%, 77.4%/40.8%, 79.7%/36.3%, and 18.1%/15.1%, respectively. The residual phase distribution, after being corrected by ICON-D2, more closely resembles the standard normal distribution, indicating a more stable correction process. The spatial distribution of the residual phases suggests that the interferograms corrected by NWMs all show signs of introducing new errors. Notably, the central positions of the interferograms corrected by both ICON-D2 and GACOS exhibit a significant phase increment. In contrast, the residual phases corrected by ERA5 and MERRA2 are better distributed, with less noise introduced. For example, although the STD of the correction by ERA5 is not as good as that by GACOS, the ERA5 method outperforms the GACOS method in the area of the first black box. However, the MERRA2 method only performs poorly at the location of the second black box. This discrepancy might be due to the limited capability of the low-resolution MERRA2 to capture small-scale tropospheric variations. In the Paris area, characterized by flat terrain, the interferograms corrected by NWMs do not exhibit tropospheric delay related to altitude. In summary, when there is a deviation between the ZTD calculated by the NWMs and the true atmospheric state, it will not only fail to reduce the delay in the interferogram but also introduce additional errors in some areas. Among them, the interferograms corrected by high-resolution NWMs are more significantly affected.

2) Correction Results in Berlin: To better analyze the correction effects of atmospheric models with different resolutions in plains, we selected the Berlin area as an example for validation due to its geographical and geomorphological similarity to Paris. The distribution of case IF03 residual phases is illustrated in Fig. 5. The large-scale air and water vapor transport induced by geostrophic flow and atmospheric circulation determines a noticeable azimuthal trend in the large-scale component. From the original interferogram before correction [see Fig. 5(a)], it is evident that the large-scale component induces a prominent northeast–southwest orientation trend, resulting in a change in the residual phase difference of nearly 40 rad. The corrected

interferograms show that all four methods better correct the northeast and southwest parts, yet residual errors persist, primarily in the southwest part. Compared with the original interferograms, the mean and STD of the corrected residuals for all four methods are reduced. ICON-D2 exhibits the best correction effect, with a 75.2% reduction in STD. GACOS, ERA5, and MERRA2 demonstrate similar residual phase distributions in this region, with performance not as effective as the ICON-D2 model. By comparing Fig. 5(e)/(g)/(i), it is evident that the high-resolution NWMs can generate more small-scale details compared with low-resolution models. Although the ICON-D2 model is more effective, some participation errors still exist in certain areas. In conjunction with the correction effects observed in the Paris region, it is evident that ICON-D2 demonstrates superior improvement in plain areas compared with other atmospheric models.

Combining the two case studies, it is evident that atmospheric models with varying resolutions can effectively address the spatial large-scale delay component. Furthermore, higher resolution atmospheric models are capable of accurately capturing more nuanced small-scale atmospheric conditions. When the NWMs calculate the ZTD with deviations from the actual atmospheric state, an "overcorrection" issue arises. This issue not only fails to reduce the delays present in the interferograms but also introduces new errors in certain regions. Notably, the interferograms that have been corrected by high-resolution NWMs are particularly affected.

3) Correction Results in Milan: As mentioned earlier, InSAR tropospheric delay is influenced by topographic relief with different dominant factors. To assess the corrective effect of NWMs on the mixing of vertical stratification delay and turbulent delay, the Milan area is chosen as a case study for synthesis in this study, considering the combination of mountains and plains in the region. Fig. 6 displays the residual phase distribution of case IF05 in the Milan area before and after correction based on different methods. Compared with the original interferogram, all four tropospheric correction methods show varying degrees of improvement. However, the final effect is consistent with the cases mentioned earlier: ICON-D2 and GACOS outperform EAR5 and MERRA2. From the topographic analysis, it is observed that GACOS, ERA5, and ICON-D2 effectively alleviate elevation-related vertical stratification delay in the northern mountainous areas of the interferogram. The ERA5 method either overestimates the effect of water vapor in the Reference or underestimates it in the Secondary, leading to a change in the northwestern portion of the ERA5-corrected interferogram from blue to red. In the plains, ICON-D2 shows a better overall correction effect than the other three methods, although some correction defects are present. GACOS introduces more errors in the plains, changing the corrected interferograms from light green to light blue. Conversely, MERRA2 exhibits better correction in gentle terrain, possibly due to the lower resolution of the model introducing fewer errors. In contrast, the high-resolution ICON-D2 model yields better accuracy for tropospheric delay, indicating its significant potential for InSAR tropospheric correction in mixed terrain.

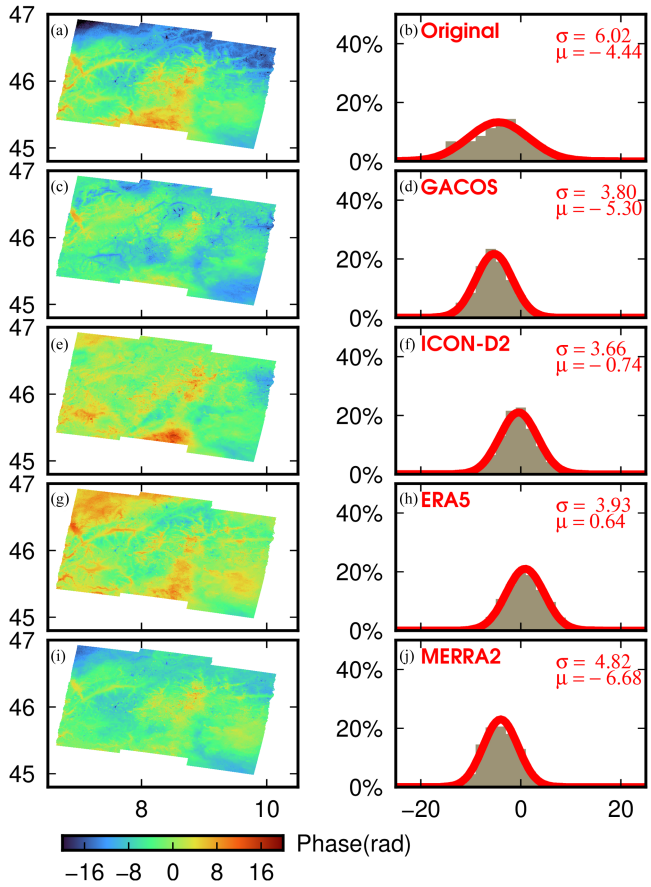

Fig. 6. Distribution of interference phases before and after tropospheric correction using different methods in Milan.

C. Assessment and Analysis of Vertical Tropospheric Delay Component

To better observe the effectiveness of different methods in alleviating the vertically stratified delay components, the distribution of phase versus elevation in the NWMs corrected interferograms was analyzed for IF05 in the Milan region, as shown in Fig. 7. The slopes of the phase versus elevation, corrected by the GACOS, ICON-D2, ERA5, and MERRA2 methods, are 0.71, 0.15, −1.52, and −1.13, respectively, with overall deviations reduced by 73.21%, 65.66%, 54.10%, and 58.70%, respectively. The phase–height relationships demonstrate that all four methods effectively correct the height-dependent tropospheric phase delay. Notably, ICON-D2 exhibits a significant correction effect on the height-dependent tropospheric phase delay. Due to its DEM-dependent interpolation method and higher quality data source, ERA5 shows better correction for the height-dependent tropospheric phase delay. MERRA2 effectively corrects the tropospheric phase delay in urban areas but falls short of completely correcting the phase delay in mountainous areas, with better correlation coefficients than ERA5. Despite GACOS having a smaller STD, both the spatial distribution of the residual phases and the elevation distribution show that there are still residual errors corrected by GACOS, which does not achieve adequate correction. The different resolution models introduce

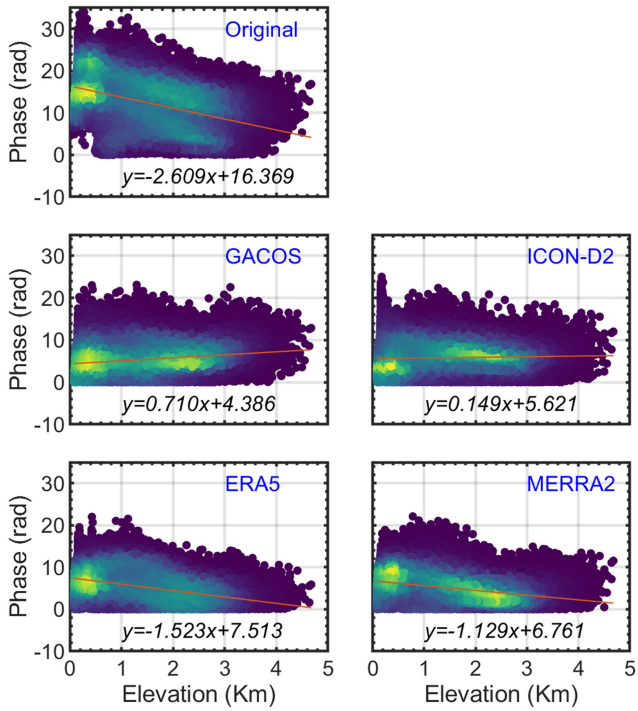

Fig. 7. Scatter plots of the phase versus elevation with least squares reference line.

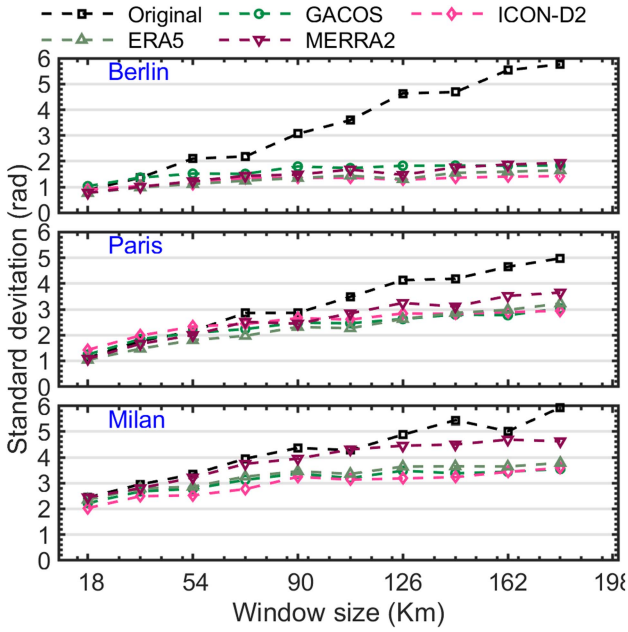

Fig. 8. Average STD as a function of the size of a square window of pixels.

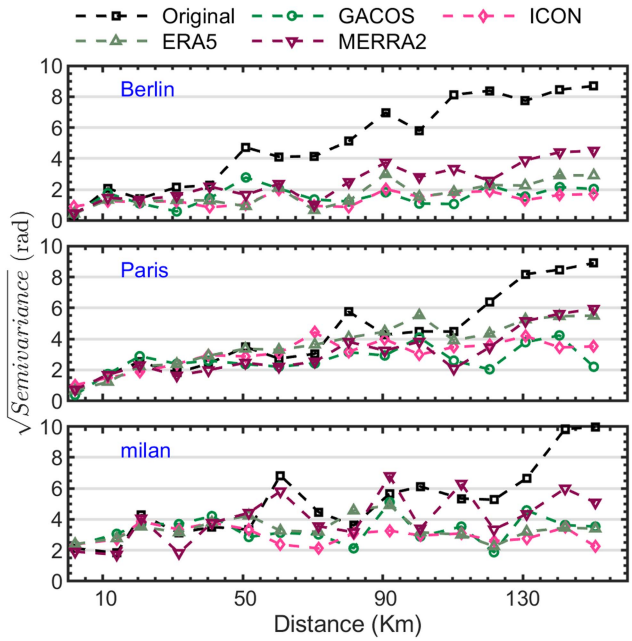

Fig. 9. Semivariograms of the residuals after correction by different NWMs.

a certain systematic bias, particularly in regions with large terrain gradients and complex geomorphology. When the model cannot accurately invert the tropospheric delay, the error introduced by higher resolution is more significant. For example, the low-resolution MERRA2-corrected residual phase distribution is smoother and introduces fewer errors.

The STD of the entire interferogram of the aforementioned experiments was assessed and analyzed in terms of temporal and spatial distribution. The reduction in the overall STD serves as a valuable metric for a rapid, comprehensive assessment of performance across all spatial scales. It is crucial to recognize that the accuracy of tropospheric delay estimation is contingent upon various factors, including the tropospheric properties within a defined region of interest, the spatial and temporal scales of said region, and the spatial/temporal resolution and accuracy of the correction dataset or model.

D. Assessment and Analysis of Different Spatial Scales

The aforementioned experiment assessed and analyzed the STD of the entire interferogram from both temporal and spatial perspectives. The overall estimation of the STD of the residual phase in the interferogram serves as a useful indicator for a quick and comprehensive assessment of the performance across all spatial scales. This also leads to the accuracy of tropospheric delay estimation being dependent on various factors, including the tropospheric characteristics of the area of interest, the spatial and temporal scales of that area, as well as the spatial and temporal resolution and accuracy of the correction dataset or model. To delve deeper into the impact of corrections at different spatial scales, we generated plots illustrating STD and semivariogram at varying spatial scales, determined by the size of the window. To fully analyze the effect of NWMs based correction, Paris: IF09, Berlin: IF10, and Milan: IF11 were used in the analysis of this experiment. The results from three regions, each characterized by different terrains, are presented in the same figure for a thorough comparison and analysis of the effects of different resolution models in InSAR tropospheric correction (refer to Figs. 8 and 9).

Fig. 8 elucidates the distributions of residual phase STD for the three regions based on different correction methods. Notably, atmospheric models with distinct resolutions exhibit

varying effects in different terrains. Across different spatial scales, ICON-D2 demonstrates the most effective correction in all three regions, particularly in the Milan area with complex terrain. GACOS and ERA5 yield comparable correction effects. As the spatial scale increases, the correction effect of the atmospheric model gradually smoothens. ICON-D2 slightly outperforms other methods in the Berlin and Paris regions with smoother topography, although the discrepancy in STD between the methods is not substantial. The ICON-D2 model demonstrates superior correction efficacy in the Milan area, characterized by more undulating terrain. The performance of MERRA2 is reversed. The current findings indicate that the high-resolution ICON-D2 is capable of capturing specific small-scale atmospheric states, yet there remains a disparity with actual turbulence delay, especially during extreme weather conditions. This suggests that, in calm weather, atmospheric models with comparable accuracy in inverted tropospheric delay exhibit limited improvement in tropospheric delay correction with increasing resolution in regions with gentle terrain. However, in complex terrain, atmospheric models with high resolution and accurate inversion of tropospheric delay demonstrate effective corrections in both vertical and horizontal delay components.

Studies have shown that spatial semivariograms offer valuable insights into the specific spatial scales that are likely to benefit from improvement and those that may not. Fig. 9 illustrates a spatial semivariogram for various regions. The correction effects at different spatial scales echo the observations from Fig. 8, but Fig. 9 provides a more distinct visualization of each method's impact across various scales. As the spatial scale increases, the magnitude of half-differences for each method rises and smoothens. Notably, MERRA2 exhibits more pronounced fluctuations with spatial scale across all regions, particularly in the Milan region, while ICON-D2 demonstrates the least variability.

In Berlin, characterized by gentle topography, atmospheric models yield similar correction effects, with positive correction noticeable from around 30 km. ICON-D2 stands out for its smoother correction trend, suggesting its superior and more robust performance across different scale spaces. Conversely, in Paris, the models exhibit limited effectiveness at all spatial scales, maintaining a consistent positive correction trend until approximately 70 km. Below 70 km, MERRA2 shows slightly better correction, potentially owing to the discrepancy between the small-scale delay quantities captured by the high-resolution model and the actual atmospheric state, introducing fewer errors compared with the low-resolution model.

The Milan area, marked by complex terrain, showcases significant performance disparities among models. ICON-D2 exhibits a stabilizing trend with increasing spatial scales, whereas ERA5 and GACOS follow similar curvilinear trends with comparable values. In contrast, MERRA2s trend varies with the original interference, suggesting persistent spatial correlation in the residual phase after tropospheric correction based on the low-resolution MERRA2. Particularly, at spatial scales below 120 km, the atmospheric phase delay remains inadequately corrected, indicating limitations in MERRA2s effectiveness in this context.

IV. Conclusion and Discussion

The application of high-precision InSAR techniques is significantly impeded by tropospheric delay. Fortunately, NWMs present a promising solution with their comprehensive temporal and spatial coverage, holding great potential for mitigating atmospheric effects in InSAR applications. This article conducts a systematic evaluation of product performance for ICON-D2, GACOS, ERA5, and MERRA2. The assessment encompasses sufficient interferograms over diverse terrains and atmospheric conditions in Berlin, Paris, and Milan. By employing European GNSS stations as a reference, the ICON-D2 model demonstrates an impressive ability to generate tropospheric delay with an accuracy of less than 1 cm, rivaling the precision of ERA5 and MERRA2. Notably, the ICON-D2 model stands out for its high accuracy and resolution within the same category of atmospheric models.

In terms of InSAR tropospheric correction, the ICON-D2 model with unassimilated GNSS ZTD shows a comparison with GACOS and is superior to both ERA5 and MERRA2. Particularly noteworthy is its enhanced correction effectiveness across varied terrains. Moreover, none of the four models can ensure long-term effectiveness in InSAR tropospheric delay correction. ICON-D2 has a better correction effect at different spatial scales, especially at low spatial scales. All four methods proficiently reproduce stratified components, with higher resolution atmospheric models exhibiting superior performance. Although high-resolution NWMs can capture more detailed features of atmospheric changes, they may introduce new errors in tropospheric delay correction if there are discrepancies from the actual atmospheric state. In some cases, high-resolution models can be less effective than coarse-resolution NWMs for InSAR atmospheric correction. The limited number of data cases in this study and the insufficient analysis of each model's spatial correction effects make it difficult to establish a definitive correction scheme. To address this issue, correction methods based on the combination of multiple NWMs should be further investigated. By analyzing the validity of interferogram residual phases corrected by different models and assigning weights based on their STDs, more accurate tropospheric delay correction phases can be achieved.

This study underscores the absence of a single method universally capable of consistently eliminating all tropospheric contributions from any given interferogram. While removing tropospheric and/or ionospheric effects enables a focused interpretation of ground displacement or surface changes, a nuanced comprehension of correction performance is imperative. The continuous assimilation of meteorological observations, particularly those with heightened spatial and temporal precision, holds promise for enhancing reanalysis performance. Future efforts concentrating on the integration of tropospheric mitigation methods and their thorough evaluation will be pivotal in fully exploiting the wealth of SAR data.

Acknowledgment

The authors would like to thank the DWD for providing the ICON model data, the GES DISC for providing MERRA2 data,

the University of Newcastle for providing data on tropospheric correction data through GACOS, and the ISCE team in JPL for providing the ISCE software package. The ERA5 data were provided by CDS.

REFERENCES

[1] S. M. Buckley, *Radar Interferometry Measurement of Land Subsidence*. Austin, TX, USA: Univ. of Texas, 2000.

[2] G. Feng, E. A. Hetland, X. Ding, Z. Li, and L. Zhang, "Coseismic fault slip of the 2008 M_w 7.9 Wenchuan earthquake estimated from InSAR and GPS measurements," *Geophysical Res. Lett.*, vol. 37, no. 1, 2010, Art. no. L01302, doi: 10.1029/2009GL041213.

[3] F. Amelung, S. Jónsson, H. Zebker, and P. Segall, "Widespread uplift and 'trapdoor' faulting on Galápagos volcanoes observed with radar interferometry," *Nature*, vol. 407, no. 6807, pp. 993–996, 2000, doi: 10.1038/35039604.

[4] M. E. Pritchard and M. Simons, "A satellite geodetic survey of large-scale deformation of volcanic centres in the central Andes," *Nature*, vol. 418, no. 6894, pp. 167–171, 2002, doi: 10.1038/nature00872.

[5] F. Dogru, F. Albino, and J. Biggs, "Weather model based atmospheric corrections of Sentinel-1 InSAR deformation data at Turkish volcanoes," *Geophysical J. Int.*, vol. 234, no. 1, pp. 280–296, 2023, doi: 10.1093/gji/ggad070.

[6] A. Singleton, Z. Li, T. Hoey, and J.-P. Muller, "Evaluating sub-pixel offset techniques as an alternative to D-InSAR for monitoring episodic landslide movements in vegetated terrain," *Remote Sens. Environ.*, vol. 147, pp. 133–144, 2014, doi: 10.1016/j.rse.2014.03.003.

[7] E. Chaussard, S. Wdowinski, E. Cabral-Cano, and F. Amelung, "Land subsidence in central Mexico detected by ALOS InSAR time-series," *Remote Sens. Environ.*, vol. 140, pp. 94–106, 2014, doi: 10.1016/j.rse.2013.08.038.

[8] M.-P. Doin, C. Lasserre, G. Peltzer, O. Cavalié, and C. Doubre, "Corrections of stratified tropospheric delays in SAR interferometry: Validation with global atmospheric models," *J. Appl. Geophys.*, vol. 69, no. 1, pp. 35–50, 2009, doi: 10.1016/j.jappgeo.2009.03.010.

[9] R. Hanssen, *Atmospheric Heterogeneities in ERS Tandem SAR Interferometry*. Delft, The Netherlands: Delft Univ. Press, 1998.

[10] H. A. Zebker, P. A. Rosen, and S. Hensley, "Atmospheric effects in interferometric synthetic aperture radar surface deformation and topographic maps," *J. Geophysical Res.*, vol. 102, no. B4, pp. 7547–7563, 1997, doi: 10.1029/96JB03804.

[11] S. Williams, Y. Bock, and P. Fang, "Integrated satellite interferometry: Tropospheric noise, GPS estimates and implications for interferometric synthetic aperture radar products," *J. Geophysical Res.*, vol. 103, no. B11, pp. 27051–27067, 1998, doi: 10.1029/98JB02794.

[12] G. Wadge et al., "Atmospheric models, GPS and InSAR measurements of the tropospheric water vapour field over Mount Etna," *Geophysical Res. Lett.*, vol. 29, no. 19, pp. 11-1–11-4, 2002, doi: 10.1029/2002GL015159.

[13] Z. Li, P. Pasquali, A. Cantone, A. Singleton, G. Funning, and D. Forrest, "MERIS atmospheric water vapor correction model for wide swath interferometric synthetic aperture radar," *IEEE Geosci. Remote Sens. Lett.*, vol. 9, no. 2, pp. 257–261, Mar. 2012, doi: 10.1109/LGRS.2011.2166053.

[14] Z. W. Li et al., "Correcting atmospheric effects on InSAR with MERIS water vapour data and elevation-dependent interpolation model," *Geophysical J. Int.*, vol. 189, no. 2, pp. 898–910, 2012, doi: 10.1111/j.1365-246X.2012.05432.x.

[15] Z. Li, J.-P. Muller, P. Cross, and E. J. Fielding, "Interferometric synthetic aperture radar (InSAR) atmospheric correction: GPS, moderate resolution imaging spectroradiometer (MODIS), and InSAR integration," *J. Geophysical Res.*, vol. 110, no. B3, 2005, Art. no. B03410, doi: 10.1029/2004JB003446.

[16] Z. Li, E. J. Fielding, P. Cross, and R. Preusker, "Advanced InSAR atmospheric correction: MERIS/MODIS combination and stacked water vapour models," *Int. J. Remote Sens.*, vol. 30, no. 13, pp. 3343–3363, 2009, doi: 10.1080/01431160802562172.

[17] L. Qiu, P. Chen, Y. Yao, H. Chen, F. Tang, and M. Xiong, "An interferometric synthetic aperture radar tropospheric delay correction method based on a global navigation satellite system and a backpropagation neural network: More suitable for areas with obvious terrain changes," *Sensors*, vol. 23, no. 24, Dec. 2023, Art. no. 9760, doi: 10.3390/s23249760.

[18] Z. Zhang, Y. Lou, W. Zhang, H. Wang, Y. Zhou, and J. Bai, "Assessment of ERA-interim and ERA5 reanalysis data on atmospheric corrections for InSAR," *Int. J. Appl. Earth Observ. Geoinf.*, vol. 111, Jul. 2022, Art. no. 102822, doi: 10.1016/j.jag.2022.102822.

[19] S. N. Sailellah and Y. Fukushima, "Comparison of tropospheric delay correction methods for InSAR analysis using a mesoscale meteorological model: A case study from Japan," *Earth, Planets Space*, vol. 75, no. 1, Feb. 2023, Art. no. 18, doi: 10.1186/s40623-023-01773-z.

[20] Q. Liu, Q. Zeng, and Z. Zhang, "Evaluation of InSAR tropospheric correction by using efficient WRF simulation with ERA5 for initialization," *Remote Sens.*, vol. 15, no. 1, Jan. 2023, Art. no. 273, doi: 10.3390/rs15010273.

[21] C. Yu, Z. Li, N. T. Penna, and P. Crippa, "Generic atmospheric correction model for interferometric synthetic aperture radar observations," *JGR Solid Earth*, vol. 123, no. 10, pp. 9202–9222, 2018, doi: 10.1029/2017JB015305.

[22] X.-L. Ding, Z.-W. Li, J.-J. Zhu, G.-C. Feng, and J.-P. Long, "Atmospheric effects on InSAR measurements and their mitigation," *Sensors*, vol. 8, no. 9, pp. 5426–5448, Sep. 2008, doi: 10.3390/s8095426.

[23] Z. Lu and J. T. Freymueller, "Synthetic aperture radar interferometry coherence analysis over Katmai volcano group, Alaska," *J. Geophysical Res.*, vol. 103, no. B12, pp. 29887–29894, 1998, doi: 10.1029/98JB02410.

[24] R. Jolivet, R. Grandin, C. Lasserre, M.-P. Doin, and G. Peltzer, "Systematic InSAR tropospheric phase delay corrections from global meteorological reanalysis data," *Geophysical Res. Lett.*, vol. 38, no. 17, 2011, Art. no. L17311, doi: 10.1029/2011GL048757.

[25] Y. Wang, L. Chang, W. Feng, S. Samsonov, and W. Zheng, "Topography-correlated atmospheric signal mitigation for InSAR applications in the Tibetan plateau based on global atmospheric models," *Int. J. Remote Sens.*, vol. 42, no. 11, pp. 4361–4379, Jun. 2021, doi: 10.1080/01431161.2021.1892856.

[26] Y. Cao, S. Jónsson, and Z. Li, "Advanced InSAR tropospheric corrections from global atmospheric models that incorporate spatial stochastic properties of the troposphere," *JGR Solid Earth*, vol. 126, no. 5, May 2021, Art. no. e2020JB020952, doi: 10.1029/2020JB020952.

[27] Y. Zhao, X. Zuo, Y. Li, S. Guo, J. Bu, and Q. Yang, "Evaluation of InSAR tropospheric delay correction methods in a low-latitude alpine canyon region," *Remote Sens.*, vol. 15, no. 4, Feb. 2023, Art. no. 990, doi: 10.3390/rs15040990.

[28] J. Foster, J. Kealy, T. Cherubini, S. Businger, Z. Lu, and M. Murphy, "The utility of atmospheric analyses for the mitigation of artifacts in InSAR," *JGR Solid Earth*, vol. 118, no. 2, pp. 748–758, 2013, doi: 10.1002/jgrb.50093.

[29] P. A. Rosen et al., "The InSAR scientific computing environment 3.0: A flexible framework for NISAR operational and user-led science processing," in *Proc. IEEE Int. Geosci. Remote Sens. Symp.*, 2018, pp. 4897–4900, doi: 10.1109/IGARSS.2018.8517504.

[30] R. M. Goldstein, H. A. Zebker, and C. L. Werner, "Satellite radar interferometry: Two-dimensional phase unwrapping," *Radio Sci.*, vol. 23, no. 4, pp. 713–720, 1988, doi: 10.1029/RS023i004p00713.

[31] C. W. Chen and H. A. Zebker, "Network approaches to two-dimensional phase unwrapping: Intractability and two new algorithms," *J. Opt. Soc. Amer. A*, vol. 17, no. 3, pp. 401–414, Mar. 2000, doi: 10.1364/JOSAA.17.000401.

[32] H. Hersbach et al., "The ERA5 global reanalysis," *Quart. J. Roy. Meteorol. Soc.*, vol. 146, no. 730, pp. 1999–2049, 2020, doi: 10.1002/qj.3803.

[33] L. Huang, L. Guo, L. Liu, H. Chen, J. Chen, and S. Xie, "Evaluation of the ZWD/ZTD values derived from MERRA-2 global reanalysis products using GNSS observations and radiosonde data," *Sensors*, vol. 20, no. 22, Nov. 2020, Art. no. 6440, doi: 10.3390/s20226440.

[34] Y. Chen, Z. Li, L. Bai, J.-P. Muller, J. Zhang, and Q. Zeng, "Successful applications of generic atmospheric correction online service for InSAR (GACOS) to the reduction of atmospheric effects on InSAR observations," *J. Geodesy Geoinf. Sci.*, vol. 4, no. 1, pp. 109–115, 2021.

[35] C. Yu, N. T. Penna, and Z. Li, "Generation of real-time mode high-resolution water vapor fields from GPS observations," *JGR Atmos.*, vol. 122, no. 3, pp. 2008–2025, Feb. 2017, doi: 10.1002/2016JD025753.

[36] G. Zängl, D. Reinert, P. Rípodas, and M. Baldauf, "The ICON (ICOsahedral non-hydrostatic) modelling framework of DWD and MPI-M: Description of the non-hydrostatic dynamical core," *Quart. J. Roy. Meteorol. Soc.*, vol. 141, no. 687, pp. 563–579, 2015, doi: 10.1002/qj.2378.

[37] K. Wilgan, G. Dick, F. Zus, and J. Wickert, "Tropospheric parameters from multi-GNSS and numerical weather models: Case study of severe precipitation and flooding in Germany in July 2021," *GPS Solutions*, vol. 27, no. 1, 2023, Art. no. 49, doi: 10.1007/s10291-022-01379-0.
[38] R. Jolivet et al., "Improving InSAR geodesy using global atmospheric models," *JGR Solid Earth*, vol. 119, no. 3, pp. 2324–2341, 2014, doi: 10.1002/2013JB010588.
[39] M. Bevis, S. Businger, T. A. Herring, C. Rocken, R. A. Anthes, and R. H. Ware, "GPS meteorology: Remote sensing of atmospheric water vapor using the global positioning system," *J. Geophysical Res.*, vol. 97, no. D14, 1992, Art. no. 15787, doi: 10.1029/92JD01517.
[40] K. D. Murray, D. P. S. Bekaert, and R. B. Lohman, "Tropospheric corrections for InSAR: Statistical assessments and applications to the Central United States and Mexico," *Remote Sens. Environ.*, vol. 232, 2019, Art. no. 111326, doi: 10.1016/j.rse.2019.111326.
[41] R. F. Hanssen, *Radar Interferometry: Data Interpretation and Error Analysis*, vol. 2. Berlin, Germany: Springer, 2001.

Yongchao Ma received the M.S. degree in geodesy and survey engineering from the Xi'an University of Science and Technology, Xi'an, China, in 2020. He is currently working toward the Ph.D. degree in aeronautical and astronautical science and technology with the Harbin Institute of Technology Shenzhen, Shenzhen, China.

His current research activities are related to tropospheric delay correction for precise GNSS application, and multisource geodesy data processing and analysis.

Tong Liu received the master's degree in space physics from Shandong University, Weihai, China, in 2019, and the Ph.D. degree in aeronautical and astronautical science from the Harbin Institute of Technology, Shenzhen, China, in 2023.

He is currently a Research Associate with The Hong Kong Polytechnic University, Hong Kong. His current research interests include GNSS-based remote sensing, ionospheric disturbances, and their impact on GNSS positioning and navigation.

Zhibin Yu received the B.S. degree in space physics from the University of Science and Technology of China, Hefei, China, in 2009, and the Ph.D. degree in aerospace engineering sciences from the University of Colorado Boulder, Boulder, CO, USA, in 2014.

He is currently an Associate Professor with the Institute of Space Science and Applied Technology, Harbin Institute of Technology Shenzhen, Shenzhen, China. His research interests include atmosphere and ionosphere dynamics, and remote sensing technology development.

Chaowei Jiang received the Ph.D. degree in space physics from the University of Chinese Academy of Sciences, Beijing, China, in 2011.

He is currently a Professor with the Institute of Space Science and Applied Technology, Harbin Institute of Technology Shenzhen, Shenzhen, China. His research interests include theoretical and numerical modeling on solar eruptive activities.

Zhiping Lu received the Doctorate degree in geodesy and survey engineering from Wuhan University, Wuhan, China, in 2001.

He is a Professor and a Doctoral Supervisor of Information Engineering University, Zhengzhou, China. His research interests include the GNSS positioning and the theory of terrestrial reference frame.